Minimizing Errors Associated with Multiplate Radiation Shields

SCOTT J. RICHARDSON AND FRED V. BROCK

School of Meteorology, University of Oklahoma, Norman, Oklahoma

STEVEN R. SEMMER AND CATHY JIRAK

National Center for Atmospheric Research, Boulder, Colorado

22 December 1997 and 1 February 1999

ABSTRACT

Multiplate radiation shield errors are examined using the following techniques: 1) ray tracing analysis, 2) wind tunnel experiments, 3) numerical flow simulations, and 4) field testing. The authors' objectives are to develop guidelines for radiation shield and temperature sensor design, to build an improved shield, and to determine factors that influence radiational heating errors. Guidelines for reducing radiational heating errors are given that are based on knowledge of the temperature sensor to be used, with the shield chosen to match the sensor design.

A new class of shield called a part-time aspirated multiplate radiation shield is introduced. This type of shield consists of a multiplate design usually operated in a passive manner but equipped with fan-forced aspiration capability to be used when necessary (e.g., low wind speed). A prototype shield reduced radiational heating errors from 2° to 1.2°C. In addition, nighttime low wind speed errors were reduced from 1.6° to 0.3°C. Existing passive shields may be modified to incorporate part-time aspiration, thus making them cost effective.

1. Introduction

Multiplate radiation shields, without a fan to augment air flow, are used to protect air temperature sensors when power consumption is a constraint. Some examples, the Gill shield and a shield denoted N221E (see section 2), are illustrated in Figs. 1a and 1b. Their use is common in mesoscale networks such as the National Center for Atmospheric Research Portable Automated Mesonet (Brock and Govind 1977; Brock et al. 1986) and the Oklahoma Mesonet (Brock et al. 1995). With good temperature sensors and electronic design, the greatest source of air temperature measurement error is exposure error due to inadequate coupling with the atmosphere. This is not a new observation; Albrecht (1927, 1934) documented the phenomenon of excess temperature due to solar radiation. When wind speeds decrease below 1–2 m s^{-1} in a multiplate shield, temperature errors in excess of 1°C are not uncommon (Tanner et al. 1996). An extreme example of radiation-induced errors is shown in Fig. 2, taken from wind tunnel experiments conducted by Gill (1979).

A good shield design 1) minimizes radiation reaching the sensor, 2) minimizes radiation absorbed by the shield, and 3) maximizes ambient air flow around the sensor. Because the three shield design criteria interact to some extent (e.g., increased protection from radiation may result in decreased airflow around the sensor), one cannot be optimized without regard to the others. Further, optimal design is a function of the characteristics of the enclosed sensor, such as absorptivity and radius, and also of the local climatology.

Objectives of this paper are to develop guidelines for radiation shield and temperature sensor design, to build an improved shield, and to determine what factors influence radiational heating errors. This is accomplished using ray tracing, wind tunnel tests, numerical simulations, and field tests.

2. The shield

Our research focused on the standard passive multiplate shield due to common constraints on available power and local climatology. We chose the Gill passive shield as a starting point and tested variations based on this design. This includes a new plate designed to reduce radiation effects and the addition of forced ventilation to a multiplate passive shield.

The N221E shield (Fig. 1b) is designed to minimize solar radiation reaching the temperature sensor. The basic Gill plate shape is altered such that the overlap from

Corresponding author address: Scott J. Richardson, Oklahoma Climatological Survey, 100 East Boyd St., Suite 1210, Norman, OK 73019-0628.
E-mail: scott@ou.edu

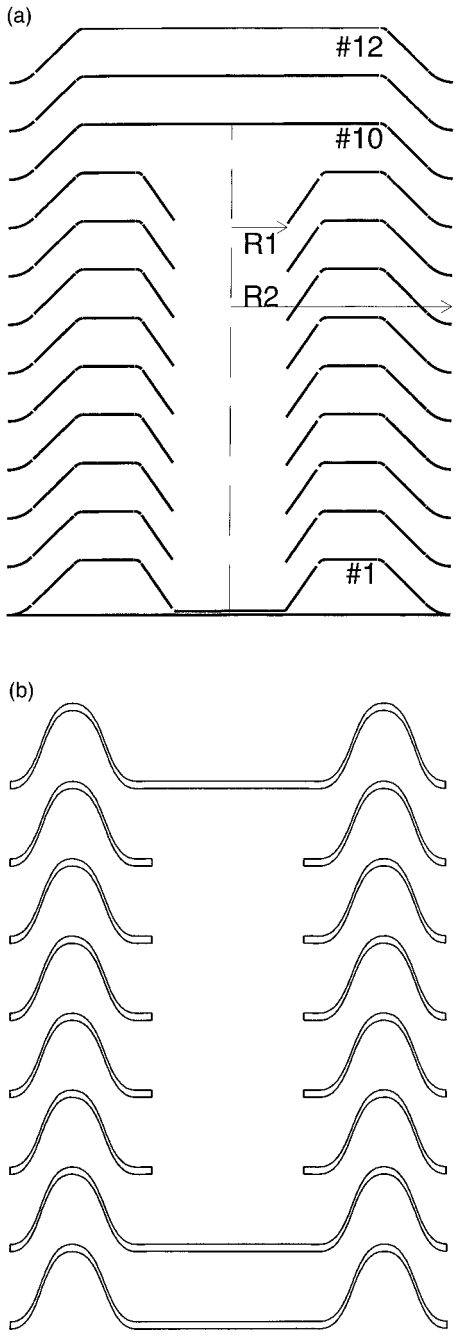

FIG. 1. (a) Cross section of a Gill multiplate shield. Plates are numbered from the bottom (1) to the top (12) and discussed in the text. The inner and outer radii of the shield are R1 and R2. (b) Cross section of a new radiation shield designated N221E. The shield has parabolic-shaped plates and is considerably better than the Gill shield at preventing radiation from reaching the sensor. However, it blocks more flow than the Gill shield.

the top of one plate to the bottom of the one above is reduced to just 2 mm, the approximate thickness of the plate. In addition, all eight plates are identical.

To overcome the poor performance of a passive shield in low winds and/or high global solar radiation, a multiplate design is modified in which a small DC axial van, Micronel V301M, is inserted into the central opening of the shield. The fan is positioned above the temperature sensor and designed to draw air across the sensor. It was quickly determined that little air passed across the sensor due to the openness of the shield. Therefore, the airflow was reversed to blow directly across the sensor and this provided adequate airflow. This introduced additional heating due to the fan's motor and tests were conducted to determine the increase in temperature due to this heating. Results indicated a 0.18°C increase at ambient temperature below 30°C, and approximately 0.25° at 50°C. The temperature increase due to the fan is acceptable because the intention is to use the fan only when temperature errors are in excess of approximately 1°C.

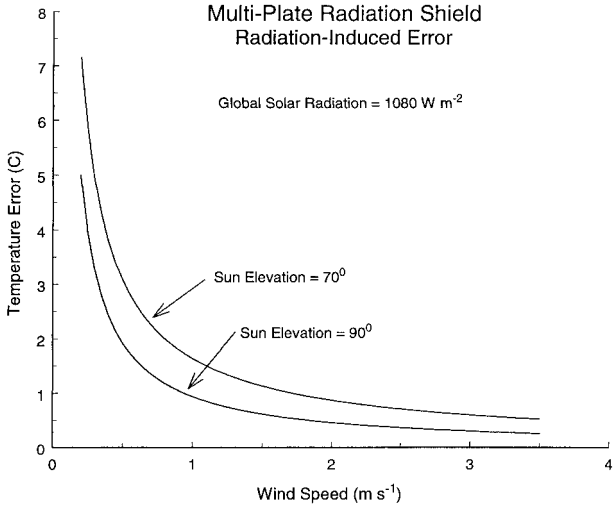

FIG. 2. Excess temperature error measured by G. C. Gill in a wind tunnel.

3. Shield testing

a. Optical ray tracing

Radiation striking the shield is partly reflected away from the shield and partly absorbed by the shield plates, and the sensor inside the shield absorbs the remainder. We defined radiation efficiency as the fraction of radiation incident on a shield from a specified angle that is blocked (by reflection or absorption) from reaching the sensor. To optimize radiation efficiency, the shield must be designed to protect the sensor from incoming radiation, primarily solar radiation. Ray tracing addresses this problem, as well as absorption of radiation by the shield, by determining the distribution of absorbed incoming radiation throughout the shield and over the sensor surface.

A ray tracing program was written to trace rays from the sun to and through the radiation shield to estimate the radiative power absorbed by various shield plates

and by the sensor inside. The program traces rays in two dimensions: *R*, the shield radial, and *Z*, the shield height. This code is limited to radially symmetric, multiplate shields such as the Gill shield, with a cylindrical sensor located along the centerline. The wavelength-dependent shield and/or sensor absorptivity is examined by running the program with various shield and/or sensor absorptivities.

Since a real plate surface is not perfectly smooth, the reflections will not be exactly specular, and, therefore, at each reflection a single ray can be scattered into multiple rays with slightly different angles. To simulate this, a random angle with a Gaussian distribution is added to the calculated specular reflection angle. By launching many different rays from the same location or by launching many closely spaced rays, the program approximates nonspecular reflections. The user specifies the standard deviation of the random angle; if the standard deviation is zero, reflection will be specular. Results are not very sensitive to the choice of the standard deviation.

At each reflection from a surface, a ray losses power equal to its current intensity times the surface absorptivity times the cross-sectional width of the surface. Ray width is taken to be the width of the shield or the width of the sensor.

Rays are launched with source angles ranging from −89° to 89°, where 0° indicates a horizontal ray and 90° is the sun directly overhead. Negative angles indicate radiation reflected from below. Primary program output is the power absorbed by each plate and the power absorbed by the sensor as a function of the source angle. This is modulated by the desired source strength.

A shield with a radiation efficiency of 1.0 does not allow any radiation to reach the sensor, but it will not be a useful design if it blocks airflow. An efficiency of 0.0 indicates the shield is not providing protection. Typical shield efficiencies range from 0.5 to 1.0 and vary considerably as a function of the angle of incidence. Figure 3 is a plot of the calculated radiation efficiency as a function of solar angle for the Gill shield. The plot must be interpreted using some estimate of the relative power density as a function of solar angle.

In an attempt to minimize the flux of solar radiation reaching the sensor, shield N221E was designed. Ray tracing indicated that the radiation efficiency for N221E is better than that for the Gill design; average efficiency for positive angles increased from 0.86 for the Gill to 0.97 for N221E. For negative angles the average efficiency increased from 0.72 for the Gill to 0.91 for N221E. Both shields are most sensitive to radiation coming from negative angles. The amount of energy reflected from below is a function of the ground cover and can be highly reflective for snow and dry sand or rather low over a grass-covered surface.

The ray tracing program was used to map the radiation received along the shield axis, as if the sensor extended all the way from the bottom shield plate to the inside top of the shield. In the shield cross section

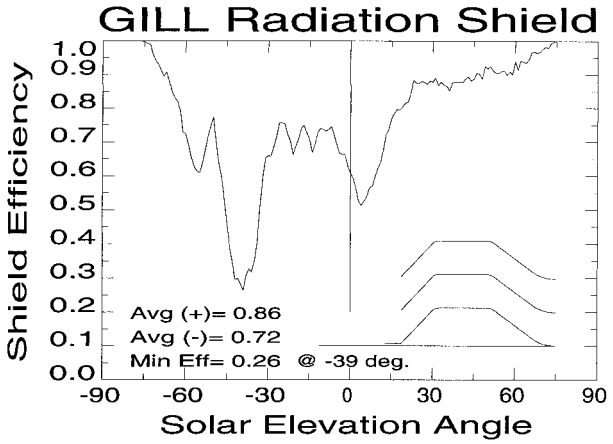

FIG. 3. Calculated radiation efficiency of the Gill shield. The average for positive angles of incident radiation is 0.86 and 0.72 for negative angles.

in Fig. 1a, plates 1–9 dip down near the center but plate 10 does not. Ray tracing showed this causes a radiation ''hot spot'' just below plate 10 because rays entering the shield between plates 9 and 10 can reach the centerline with fewer reflections than rays entering between lower plates.

Tests indicate that for incident rays that do not bounce clear of the shield after the first reflection, the shield acts almost like a blackbody irrespective of the shield absorptivity. Put another way, ray tracing shows that no matter where a ray goes after initial shield entry, on average, most of its energy will be lost to the shield or to the sensor. This is an undesirable characteristic because the radiative energy absorbed by the shield may eventually cause radiational heating errors.

b. Wind tunnel experiments

Two sets of wind tunnel experiments were conducted: one to measure the flow speed inside the shield and another to measure the temperature rise of a sensor inside the shield as a function of external radiational heating and external flow speed. The National Center for Atmospheric Research (NCAR) wind tunnel was used to evaluate the Gill multiplate shield (as built by R. M. Young) and the N221E shield. Airflow inside the shield, on the vertical shield axis, was measured using a Thermo Systems Inc. model 8470 omnidirectional, hot-film air velocity transducer with a 2-mm-diameter sensing head. The wind profile along the shield axis was measured for various external flow rates starting at 1 m s^{-1}. Excess temperature, air temperature inside the shield minus the air temperature at a point upstream from the shield, was measured using YSI 44006 bead thermistors under various wind speed conditions, while illuminating the shield with a strong light source (projecting 630 w m^{-2} on the shield). Both transducer probes were moved ver-

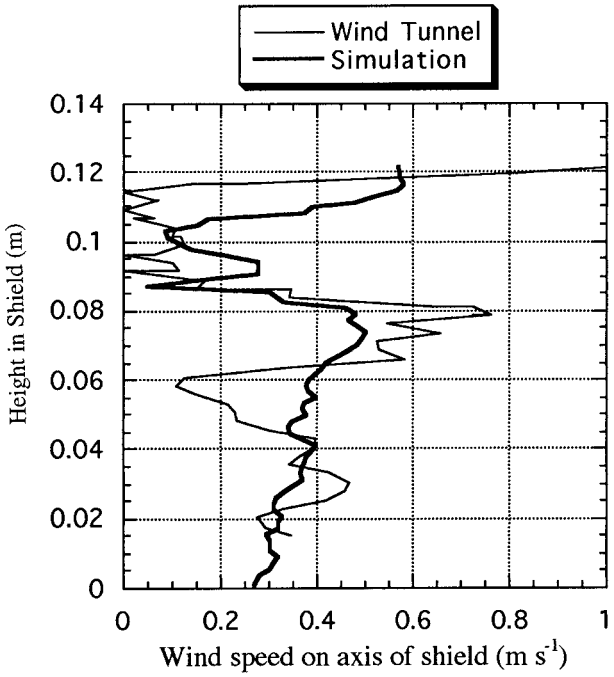

FIG. 4. Wind speed as a function of height through the center of a Gill multiplate shield. Ambient flow was 1 m s^{-1}. ''Wind tunnel'' represents data obtained from wind tunnel measurements and ''Simulation'' is data from a 2D numerical simulation.

tically inside the shield to measure either temperature or wind speed profiles.

1) FLOW MEASUREMENT INSIDE THE SHIELDS

A flow profile inside the Gill shield is shown in Fig. 4 for an external speed of 1 m s^{-1}. Measurements were made without a temperature sensor in the shield. The profile is irregular, showing that the local maxima between the plates drops below 0.1 m s^{-1} from 90 to 110 mm. There is a 1 m s^{-1} ''jet'' just under plate 10 (Fig. 1a). This plate does not dip down in the center, as do the others below it, so it offers less flow resistance. The average internal flow speed was 0.3 m s^{-1} when the external speed was 1.0 m s^{-1}. The presence of a secondary jet between 60 and 80 mm and the minima between 90 and 110 mm suggests the possibility of a local circulation cell in the center of the shield where the sensor would be located. This hypothesis was supported by results from numerical simulations (section 4). Ray tracing shows there is a radiation hot spot coincident with the jet under plate 10, so it is not recommended to locate a sensor in this region.

Flow profile measurements were made inside the N221E shield and the average flow speed at a tunnel speed of 0.89 m s^{-1} was 0.2 m s^{-1}. This is a 50% decrease from the Gill shield design (when the external speed is 1 m s^{-1}). The N221E shield was better than the Gill shield in protecting the sensor from radiation; however, it had a lower flow efficiency.

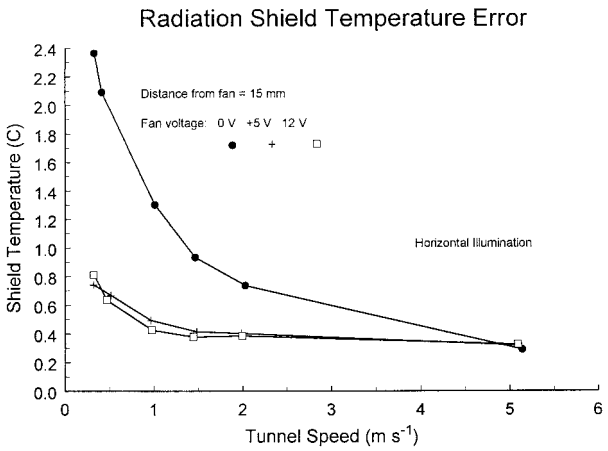

FIG. 5. Excess temperature measured inside shield N221E.

2) TEMPERATURE MEASUREMENT

The N221E shield with the small fan was used in the temperature measurements. Excess temperature in the N221E shield was measured over a vertical profile and at each height the supply voltage to the fan was varied between 12 V, nominal voltage, and 5 V. This was done to determine if the fan could be effective at the lower voltage to conserve power. Figure 5 shows the excess temperature error with the sensor 15 mm away from the fan. The solid upper curve in Fig. 5 is the excess temperature with the fan off; with the fan on, the temperature error was significantly reduced. The fan was equally effective at 5 V (in the wind tunnel) as at 12 V. When the fan was blowing away from the sensor, the temperature error was equivalent to the fan-off curve regardless of the fan voltage.

Excess temperature measurements inside the Gill shield were not available.

c. Numerical flow simulation

Wind tunnel experiments, such as those described here, provide a direct measure of the wind speed inside a shield. However, using such techniques requires a prototype shield to be constructed, an expensive proposition. Numerical simulations provide an alternate method for examining flow through shields. In addition, numerical simulations provide more detailed information about the flow characteristics inside the shield than are possible from wind tunnel testing and numerous shield shapes can be tested with relative ease.

A detailed description of the model along with the validation tests that were performed can be found in Richardson (1995b,c). The required vertical and horizontal resolutions were discussed there in the context of boundary layer theory to ensure that the shearing stresses were adequately resolved. To summarize, minimum horizontal and vertical resolution were determined by simulating a Blasius boundary layer (Schlicht-

ing 1979) and by examining the friction coefficient (or local drag) along a flat plate (Kreith and Bohn 1993). It was found that the boundary layer velocity profile was adequately resolved when the first grid point was 1 mm from shield surfaces and when 1-mm gridpoint spacing was used on the shield. Simulations using a finer grid resulted in the same solution, demonstrating that a grid-independent solution had been obtained.

1) DESCRIPTION OF NUMERICAL MODEL

The model used to perform the simulations was FLUENT, by Fluent Inc., and was a general-purpose computer program for modeling fluid flow, heat transfer, and chemical reaction. The grid could be standard Cartesian coordinates, cylindrical coordinates, body-fitted curvilinear coordinates (where grid lines follow the physical geometry), or a totally unstructured grid. For the simulations shown here, unstructured grids were used because of the ease of grid generation and because local grid refinements could be made based on, for example, local velocity gradients. All simulations were performed using air as the working fluid at standard atmospheric conditions and constant density.

The 2D simulations used an x–z plane of symmetry through the center of a shield parallel to the direction of the wind vector. In general, three-dimensional simulations were not performed due to the complexity of creating the geometry and the required computer resources. Limited 3D simulations were compared with 2D simulations to ensure the latter adequately represented the flow through the center of the shield.

An example of a 2D unstructured grid used for simulating flow through a Gill shield is shown in Fig. 6a. Shield dimensions are the same as a standard Gill shield: 0.12-m diameter, with 0.16-m-high and 0.002-m-thick plates. Each triangle represents a computational cell with the most cells concentrated near the shield plates in order to represent the boundary layer shearing stresses. The entire computational domain was approximately 2.5 m long and 2.25 m high, which provided many shield diameters between the shield and boundaries to reduce their effect on the flow. Air enters the domain from the left at a specified velocity and exits the domain on the right. The top and bottom boundaries are free slip and rigid.

Figure 6b shows velocity vectors computed using a grid very similar to the one shown in Fig. 6a, with the length of the vector proportional to the velocity. Air enters the domain from the left at a speed of 1.0 m s^{-1}. Flow accelerates as it is diverted around the top (and bottom) of the shield; the vectors near the top leading edge of the shield represent the greatest velocities, 1.6 m s^{-1}. Complicated flow structures can be seen; there are numerous small circulations and areas of flow separation evident, both of which act to decrease the flow through the shield. A large circulation can be seen near the top of the shield that results from using a flat top plate.

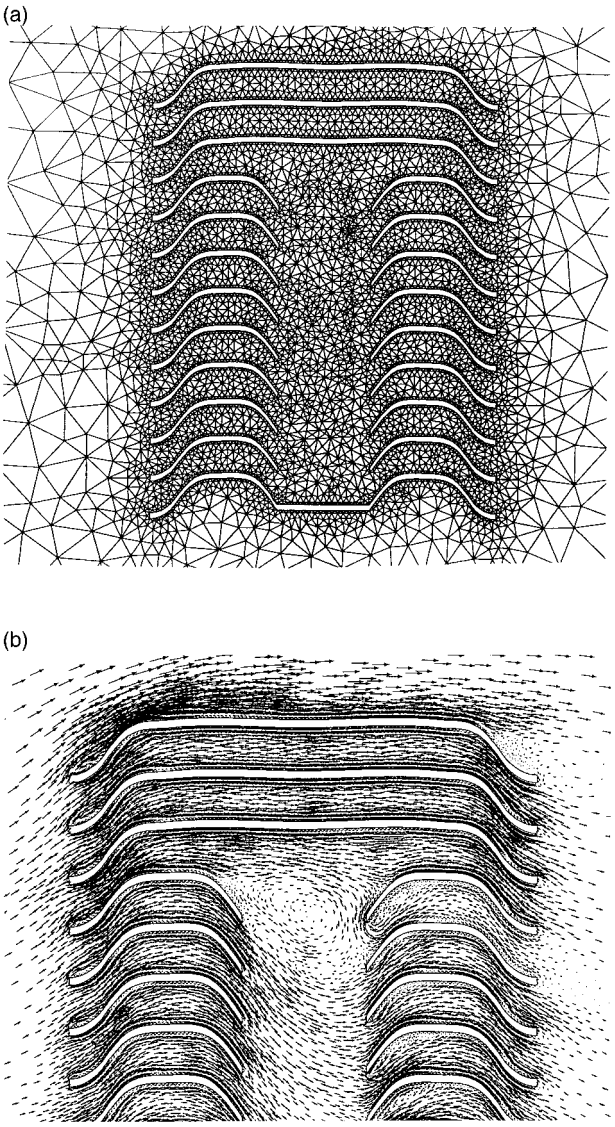

FIG. 6. (a) Unstructured grid used for flow calculations of the Gill shield. (b) Velocity vectors calculated using a grid very similar to the one shown in (a). Flow enters from the left at 1.0 m s^{-1}. Velocity magnitude is proportional to the length of the vector. The largest velocity occurs on the top leading edge of the shield and is 1.6 m s^{-1}.

If flow through a shield is to be maximized, flow separation and other obstruction to the airflow must be eliminated or minimized; Fig. 6b helps to demonstrate this problem.

2) COMPARISON OF 2D SIMULATIONS AND WIND TUNNEL RESULTS

Wind tunnel measurements are compared with numerical simulations as a means of validating the model.

Wind speed measurements made inside a standard Gill shield and N221E are used for comparison.

A plot of velocity magnitude as a function of height inside the Gill shield, as measured in the wind tunnel and as determined from a 2D simulation, is shown in Fig. 4. Ambient wind speed is 1.0 m s^{-1} in both cases. Results from the simulation show a general linear increase in wind speed from the bottom of the shield (0 m) to about 0.08 m, where the flow decreases rapidly. The flow then increases again at 0.12 m.

There is very good agreement between wind tunnel and numerical simulation results for the N221E shield in a 0.9 m s^{-1} flow. In this case, wind tunnel measurements show the flow inside the shield oscillating between approximately 0 and 0.4 m s^{-1} in between each successive set of plates. Simulations yield a very similar flow pattern, with the magnitude of the predicted flow generally within 0.1 m s^{-1} of those obtained in the wind tunnel.

The agreement between the wind tunnel measurements and the simulations is reasonable with the general flow features being captured. There are many flow obstructions present in the wind tunnel that are not represented in the simulation such as plate spacers, a shield mounting bracket required in the wind tunnel, the effects of the probe on the flow, and the potential to mount the shield slightly off vertical in the wind tunnel.

The term *flow efficiency* is used to describe the ratio of flow speed through the center of the shield (averaged over the height of the shield) to the upwind speed (outside the shield). Increasing flow efficiency usually decreases radiational heating errors because convective heat transfer is increased; however, there may be an increase in radiation reaching the sensor.

The flow efficiency for the Gill shield calculated from the wind tunnel data was 0.31 and 0.37 for the simulation. The flow efficiency for N221E calculated from the wind tunnel date (at 0.89 m s^{-1}) is 0.24 and the simulation predicted 0.23.

3) VARYING SHIELD DESIGN

To determine how the Gill and N221E shields compare with the maximum possible flow efficiency attainable using a multiplate design, a shield with dimensions the same as the Gill shield but consisting of completely flat plates was tested. Tests show that for a 1.0 m s^{-1} external wind speed, the flow efficiency of this shield is 0.60. Thus, even a simple multiplate shield results in a 40% reduction of ambient airflow inside the shield.

Next, the plate spacing of the Gill shield is increased from 0.01 to 0.013 m, which is the maximum allowed while still preventing direct radiation from reaching the sensor. This results in a modest increase in flow efficiency from 0.37 to 0.41. The Gill design is varied again by removing the downward turn at the center of the shield plates, which results in flow efficiency increasing to 0.52. Note, however, that direct radiation can reach the sensor from negative angles.

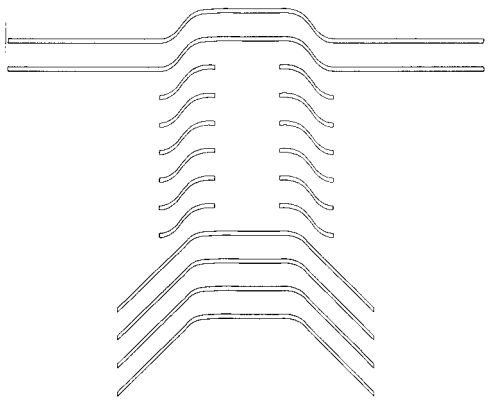

FIG. 7. New shield design, 0.22-m-diameter top plate. Flow efficiency was 0.57. Top plates are designed to shade lower plates.

The final shield to be discussed here is shown in Fig. 7 and is a variation of other shields tested. The top two plates are 0.22 m in diameter and designed to provide shade for high solar angles, while the bottom plates are designed to direct air into the shield that would otherwise be deflected under it. The flow efficiency of this shield is 0.57, which is larger than any other shield except the flat plate design. The bottom four plates are angled 45° with respect to the horizontal so that direct radiation is reflected away from, instead of into, the shield.

Numerical simulations indicate flow efficiency is a nonlinear function of external flow speed, with efficiency decreasing dramatically as wind speed decreases below 1 m s^{-1}. The nonlinearity results because the depth of the boundary layers that develop along the shield plates increase with decreasing flow speed. Figure 8 shows the flow efficiency as a function of external wind speed for the flat plate shield. Flow efficiency is fairly constant for wind speeds above 1 m s^{-1}; however, it falls off rapidly as wind speed decreases below 1 m s^{-1}. This acts to accentuate radiational heating errors, as shown in Figs. 2 and 5.

d. Field testing

A field site is used to test three different radiation shields and two different temperature sensors. Examples of radiational heating and errors associated with very low wind speed are given, and evidence is presented which supports the use of part-time aspirated multiplate radiation shields.

1) DESCRIPTION OF FIELD SITE

The site was located on a flat, open, grass field with virtually no obstructions in any direction for over 100 m; all shields were located 1.5 m above ground level. Wind speed was measured using two R.M. Young model

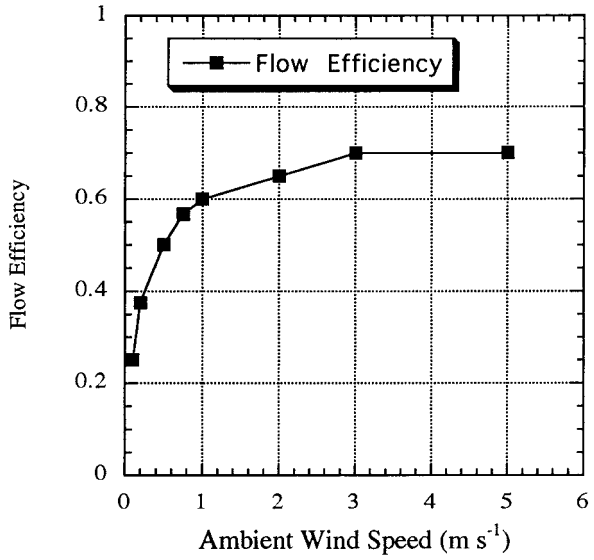

FIG. 8. Flow efficiency as a function of external wind speed for a shield with flat plates (see text). As wind speed decreases, flow efficiency decreases, especially below 1 m s^{-1}.

08274 expanded polystyrene propeller anemometers that measured the two horizontal components of the wind and were specially designed for low wind speed measurements. The propellers were mounted horizontally, facing west and south, and had start-up thresholds of approximately 0.2 m s^{-1}. The manufacturer-suggested cosine correction was applied to each wind component before calculation of the true wind vector. Global solar radiation was measured using a LI-COR pyranometer with a stated inaccuracy of $\pm 5\%$.

Temperature measurements were made from 23 April to 31 December 1994. Thermometrics model T55031/D1 temperature sensors were used in all shields except one that housed a standard Vaisala HMP 35 temperature and relative humidity sensor; this sensor was included to test for sensor-dependent radiational heating errors. The Thermometrics sensors consist of a bead thermistor exposed directly to the air. The thermistor is about 1 mm in radius and located at the end of a rugged, highly polished, stainless steel casing.

There was a fan-aspirated radiation shield (R.M. Young Model 43408) used as the reference shield and four additional test shields. Three of the shields were unmodified multiplate radiation shields (manufactured by Coastal Climate, Inc.) and one was a prototype part-time aspirated shield described in section 2. In the following discussion, the reference temperature sensor housed in the aspirated shield will be referred to as ''air temperature,'' the Vaisala sensor in the unmodified multiplate shield will be denoted as ''Vai,'' the Thermometrics sensors in the unmodified multiplate shields will be denoted by ''Therm,'' and the Thermometrics sensor housed in the prototype part-time aspirated multiplate shield will be called ''Fan.'' All data shown are 1-min averages of 3-s samples.

2) TEMPERATURE SENSOR CALIBRATION

All temperature sensors were carefully calibrated before, during, and after use in the field using the calibration method and instrumentation described in Richardson (1995a). After applying corrections to the data, residual temperature errors were less than 0.04°C for all sensors.

The *relative* accuracy of two identical Thermometrics sensors placed in identical Gill shields and separated by a distance of 5 m was examined to determine the variability of atmospheric temperature measurements. For a typical 24-h period, 95% of the temperature differences were less than 0.1°C in magnitude, while 99% were less than 0.2°C. The average temperature difference over the period was approximately −0.005°C. Thus, small radiational heating differences were detectable.

3) TEMPERATURE ERRORS DUE TO VERY LOW WIND SPEEDS

Air temperature measured by the reference sensor and wind speed measured by the propeller anemometers are shown in Fig. 9a for the period 0850 to 1000 UTC 17 August 1994. Figure 9b shows the temperature error for Vai, Fan, and Therm for this same period; wind speed is also plotted in this figure for reference. The air temperature is roughly 16°–17°C for most of the period, and the wind speed is very low with the propellers measuring zero from hour 8.9 to hour 9.3. Prior to hour 8.9, all temperature errors are less than ±0.5°C. Shortly after the winds become calm, the air temperature begins to slowly increase from 16° to almost 17.5°C, and the temperature errors for the unaspirated shields (Vai and Therm) become increasingly large, reaching −1.5°C for Therm and −1.8°C for Vai. When the wind speed increases at hour 9.3, the temperature errors for Vai and Therm begin to decrease. Note that the error for Fan, the prototype fan augmented multiplate shield, never exceeds ±0.4°C. Similar behavior can be seen at hour 9.75 when the measured wind speed is zero.

4) RADIATIONAL HEATING

The period immediately following sunrise on 7 August 1994 shows a noticeable radiational heating signal. Air temperature for this period is approximately 15.5°C before sunrise (1200 UTC) at which time it begins to increase steadily to 22.5°C by 1500 UTC. Figure 10a shows global solar radiation and wind speed for the period 1100 to 1500 UTC. Sunrise is near 1200 UTC, and global solar radiation increases steadily until hour 13, where it maintains a value of 100–200 W m^{-2} until hour 13.8. Wind speed remains below about 1 m s^{-1} for

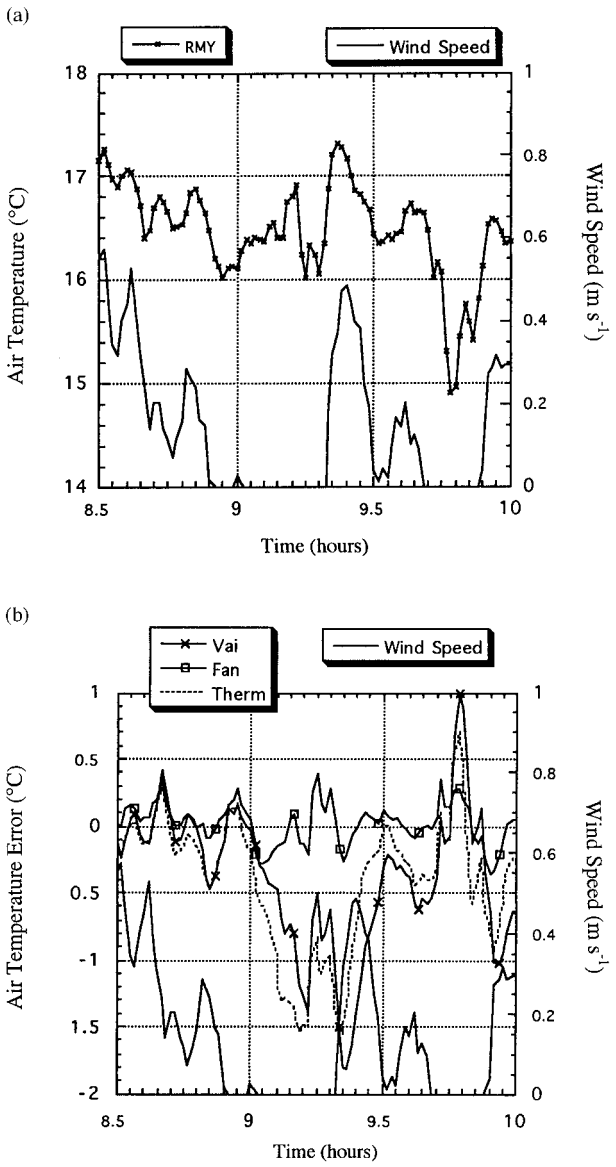

FIG. 9. (a) Air temperature and wind speed from 0830 to 1000 UTC 17 Aug 1994. (b) Same as (a) except for temperature error for Vai, Fan, and Therm sensors. Wind speed is also plotted for reference.

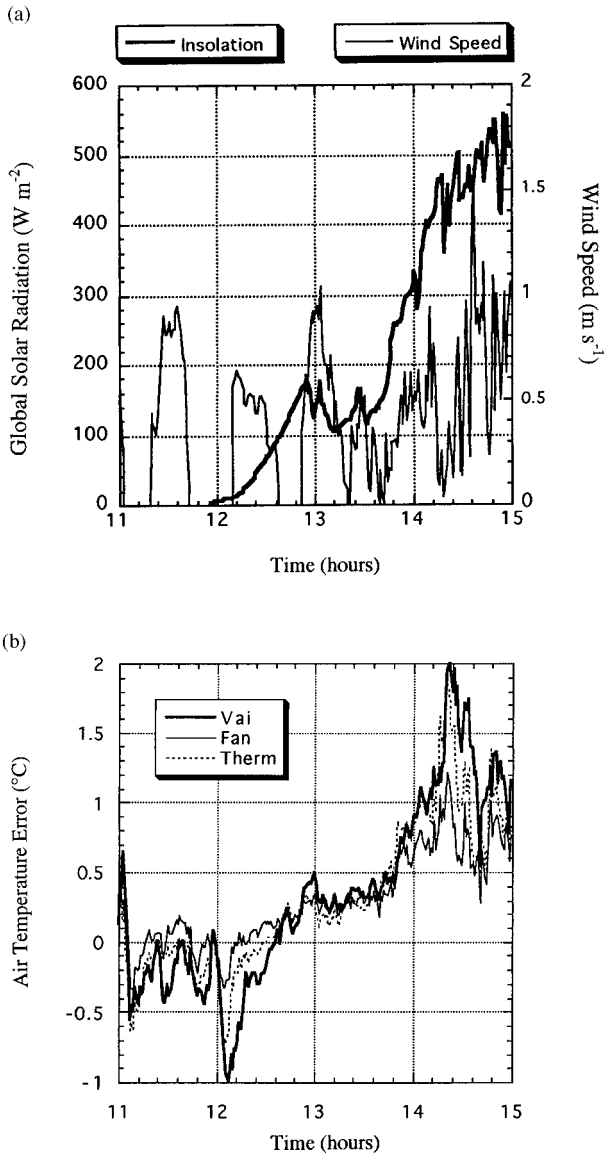

FIG. 10. (a) Global solar radiation and wind speed from 1100 to 1500 UTC 7 Aug 1994. (b) Radiational heating errors for Vai, Fan, and Therm temperature sensors.

the entire period except near hour 14.6. Temperature errors from Vai, Fan, and Therm are shown in Fig. 10b and can be seen to steadily increase from slightly negative to slightly positive between hours 12 and 13, which coincide with sunrise. Temperature errors then remain constant between hours 13 and 14, which coincide with the relatively steady value of global solar radiation during this period. Just before hour 14, global solar radiation begins to increase rapidly and temperature errors exhibit a similar behavior. Wind speeds attain a local minimum between hour 14.2 and 14.4 that coincides with the maximum temperature error of 2°C. Note that Fan had radiational heating errors approximately half those exhibited by Vai or Therm. This is additional evidence for the use of part-time aspirated shields, although a larger fan may be required. Finally, note that the increase in wind speed at hour 14.6 coincides with the decrease in radiational heating errors immediately following.

5) AVERAGED DATA

The examples given above were for short timescale events (on the order of an hour). The shield's average performance is evaluated for the period 3 August–18 December 1994. For the analysis that follows, 99 days are used because data from every minute of every day

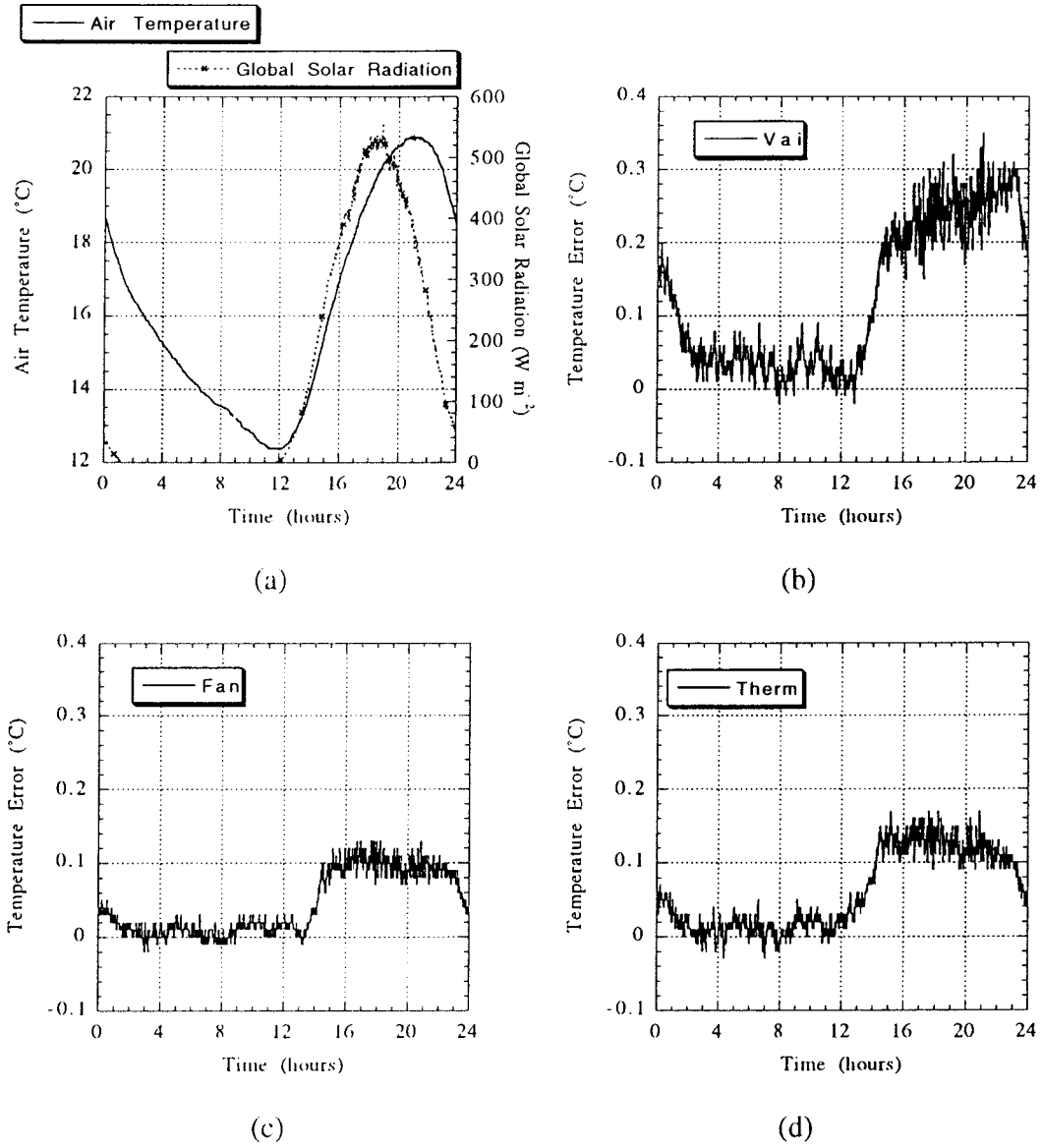

FIG. 11. Average data from 3 Aug to 18 Dec 1994. (a) Air temperature and global solar radiation, (b) Vai air temperature error, (c) Fan air temperature, and (d) Therm air temperature error.

were available. The 99 days are about equally spaced throughout the five-month period.

For the period given above, averages of all measured quantities were calculated for each minute observation. Figure 11a shows average air temperature and global solar radiation and Figs. 11b,c,d show the average temperature error for Vai, Fan, and Therm, respectively. The average wind speed for the period is not shown but was about 2 m s^{-1} at night and 3 m s^{-1} during the day. A value of 0.18°C was subtracted from the Fan air temperature because this is how much the fan heated the air (section 2).

At night, all three sensors show relatively small errors with no discernible radiational cooling effects. During daylight hours, radiational heating errors are approximately 0.2°–0.3°C for Vai, approximately 0.1°C for Fan, and approximately 0.14°C for Therm.

Although these radiational heating effects are small, the average daytime wind speed was 3 m s^{-1}, a relatively large value when examining radiational heating errors. In addition, the surface reflectivity was low as was the average maximum global solar radiation. Therefore, it seems reasonable to conclude that average radiational heating effects for some sensors in the Gill shield could be larger (0.5°–1.0°C or more) if exposed to more extreme conditions. This conclusion is supported by Tanner et al. (1996) in which a field experiment showed multiplate shield errors in excess of 1°C when wind

speeds were below 1–2 m s^{-1} and global solar radiation was in excess of 800 W m^{-2}.

4. Observations

The work summarized here describes errors associated with the use of multiplate radiation shields. A radiation shield should have low solar absorptivity and high thermal absorptivity, as described in Fuchs and Tanner (1965), to minimize shield heating. The shield surface should be smooth to minimize dirt accumulation. Field experience indicates that it is very difficult to achieve and maintain low absorptivity. Accumulation of dust and, in some locations (e.g., Oklahoma), mold and fungus act to increase absorptivity.

Optimum shield design is a function of location and climatology, and the characteristics of the sensor inside the shield. Relevant climatological characteristics include maximum solar elevation angle, ground reflectance, and probability of high radiation coupled with very low wind speeds. All of these factors stress the shield performance.

The sensor should be designed to maximize convective heat transfer and minimize radiative and conductive heat transfer. This suggests the sensor should have a small radius, fit entirely within the shield, be highly reflectivity, and have a sensing element exposed directly to the airstream. If these criteria are met, then the shield should (in descending order of importance) maximize flow past sensor, provide mechanical protection and protect the sensor from rain, provide part-time aspiration if possible, and reflect as much radiation as possible.

The Gill shield performs acceptably if the sensor does not meet the above criteria.

Ray tracing shows that the radiation efficiency of the N221E shield is considerably better than the Gill shield; however, wind tunnel measurements and numerical simulations show that the flow efficiency of N221E is considerably worse than the Gill shield.

Simulations show complex flow structures and demonstrate that small changes in plate shape and/or plate spacing produce considerably different flows inside the shield. Simulations also show that shield flow efficiency is a nonlinear function of wind speed, with efficiency decreasing as wind speed decreases.

Field testing shows examples of sensor-dependent radiational heating errors and demonstrate that part-time aspirated multiplate radiation shields can be used to dramatically reduce radiational heating and low wind speed errors. Note that the lifetime of the fan used in this study was approximately one year and, therefore, a different fan may be better suited for long-term unattended use.

Part-time aspirated shields are an inexpensive alternative to fully aspirated shields and represent a good compromise between cost, power consumption (power to the fan can be switched), accuracy, and reliability (errors associated with their use should be no larger than a standard multiplate shield if the fan fails). In addition, it is possible to modify existing passive shields to be part-time aspirated.

If it is not possible to expose the sensing element directly to the air stream, as is the case for many combination temperature and relative humidity probes, then better accuracy and considerably faster time response can achieved if a *separate* air temperature sensor, exposed directly to the air stream, is used to provide the air temperature measurements (Richardson et al. 1998).

It appears that, regardless of the passive shield design, radiational heating errors are significant when winds speeds are below 1–2 m s^{-1}. Therefore, it may prove more feasible to remove the shield than to design a better shield. That is, one could use a *very* well-designed temperature sensor (e.g., like that used on radiosondes) and a simplified shield consisting of a no more than a flat plate to provide shade for the temperature sensor. This configuration protects the sensor from most mechanical damage and moisture and shades the sensor for all but the lowest solar elevation angles. For example, a sensor placed 5 cm below a plate with a 30-cm radius should be shaded for solar elevation angles above about 9°. Obviously, the sensor is heated by radiation for low solar angles or if highly reflective surface conditions are present. However, a very small and reflective sensor is little affected by radiation (e.g., fast-response fine-wire thermocouples). A second temperature sensor housed in a traditional multiplate shield can be used for sunrise and sunset or high surface reflectivity conditions.

Throughout this paper, radiation-induced error has been characterized as exposure error to distinguish it from systematic errors and random errors, such as bias and imprecision. Most instrument errors are classified as either systematic or random and are quantified during a laboratory calibration process. Vendors report quantifiable errors and their specifications do not include exposure errors because these are not under their control. For this reason, sensor error specifications are somewhat misleading. It is easy to construct a temperature sensor that, in the laboratory, will have errors less than 0.1. However, as shown in this paper and by others (e.g., Tanner et al. 1996), it is extremely difficult to consistently achieve such high levels of performance in the field.

Acknowledgments. The authors wish to gratefully acknowledge the insight and support provided by Tom Horst and John Militzer. Thomas Foken provided the German references. The authors also acknowledge the assistance of K. K. Droegemeier, K. C. Crawford, W. H. Beasley, and R. Cox for their help in selecting, obtaining, and testing the FLUENT model. R.M. Young Co. constructed two of the part-time aspirated multiplate shields, and Sherman Fredrickson and the National Severe Storms Laboratory provided part of the instrumentation for the field site. Tim Hughes suggested incorporating a small fan inside a multiplate shield to reduce radiational heating errors. The scientists in the

Mesonet calibration laboratory provided space and equipment necessary to perform calibrations. This work was supported in part by the Oklahoma Mesonet Project operated by the Oklahoma Climatological Survey and by the ARM Program of the U.S. Department of Energy through Battelle PNNL Contract 144880-A-Q1 to the Cooperative Institute for Mesoscale Meteorological Studies. Computer time was provided by the Pittsburgh Supercomputing Center (PSC) through an educational grant from Cray Research Incorporated; Ralph Roskies, Christine Ricci, and David Oneal were instrumental in being able to perform the necessary calculations at PSC.

REFERENCES

Albrecht, F., 1927: Thermometer zur Messung der wahren Lufttemperatur. *Meteor. Z.,* **24,** 420–424.

——, 1934: Über die Einwirkung der Strahling auf frei aufgestellte elektrische Thermometer. *Veröff. Pruss. Meteor. Inst.,* **402,** 76–82.

Brock, F. V., and P. K. Govind, 1977: Portable automated Mesonet in operation. *J. Appl. Meteor.,* **16,** 299–310.

——, G. H. Saum, and S. R. Semmer, 1986: Portable automated Mesonet II. *J. Atmos. Oceanic Technol.,* **3,** 573–582.

——, K. C. Crawford, R. L. Elliott, G. W. Cuperus, S. J. Stadler, H. L. Johnson, and M. D. Eilts, 1995: The Oklahoma Mesonet: A technical overview. *J. Atmos. Oceanic Technol.,* **12,** 5–19.

Fuchs, M., and C. B. Tanner, 1965: Radiation shields for air temperature thermometers. *J. Appl. Meteor.,* **4,** 544–547.

Gill, G. C., 1979: Development of a small radiation shield for air temperature measurements on drifting buoys. Contract No. 01-7-038-827 (11), NOAA Data Buoy Office.

Kreith, F., and M. S. Bohn, 1993: *Principles of Heat Transfer*. West Publishing, 720 pp.

McTaggart-Cowan, J. D., and D. J. McKay, 1976: Radiation shields—An intercomparison. Atmospheric Environment Service of Canada. [Available from Atmospheric Environment Service, 4905 Dufferin St., Downsview, ON M3H 5T4, Canada.]

Richardson, S. J., 1995a: Temperature and relative humidity calibrations for the Oklahoma Mesonetwork. *J. Atmos. Oceanic Technol.,* **12,** 951–959.

——, 1995b: Passive solar radiation shields: Numerical simulations of flow dynamics. Preprints *Ninth Symp. on Meteorological Observations and Instrumentation,* Charlotte, NC, Amer. Meteor. Soc., 253–258.

——, 1995c: Multiplate radiation shields: Investigating radiational heating errors. Ph.D dissertation, University of Oklahoma, 134 pp.

——, S. E. Fredrickson, F. V. Brock, and J. A. Brotzge, 1998: Combination temperature and relative humidity errors: Avoiding large air temperature errors and associated relative humidity errors. Preprints, *10th Symp. on Meteorological Observations and Instrumentation,* Phoenix, AZ, Amer. Meteor. Soc., 278–283.

Schlichting, H, 1979: *Boundary-Layer Theory*. 7th ed. McGraw-Hill, 817 pp.

Tanner, B. D., E. Swiatek, and C. Maughan, 1996: Field comparisons of naturally ventilated and aspirated radiations shields for weather station air temperature measurements. Preprints, *22d Conf. on Agricultural and Forest Meteorology,* Atlanta, GA, Amer. Meteor. Soc., 227–230.